

Contents lists available at ScienceDirect

Tectonophysics

journal homepage: www.elsevier.com/locate/tecto



Effects of pre-existing faults on compaction localization in porous sandstones



Gajst Hannah^{a,b,*}, Weinberger Ram^{b,c}, Zhu Wenlu^d, Lyakhovsky Vladimir^b, Marco Shmuel^a, Shalev Eyal^b

- ^a Department of Geosciences, Tel Aviv University, Israel
- ^b Geological survey of Israel, Jerusalem, Israel
- ^c Department of Geological and Environmental Sciences, Ben Gurion University of the Negev, Beer Sheva, Israel
- d Department of Geology, University of Maryland, MD, USA

ABSTRACT

The formation of deformation bands can significantly modify the strength and transport properties of porous sedimentary rocks. Among the different types of deformation bands, compaction bands exhibit porosity reduction with little to no shear displacement. Natural compaction bands have previously been reported and studied in only a few areas. They often coexist with faults and other localized deformation structures. We mapped the geometrical relation between compaction bands, shear bands and faults in Lower Cretaceous porous sandstone at Makhtesh Katan, Israel. To understand the effect of pre-existing faults on the formation of compaction bands, we conducted deformation experiments on pre-faulted Bentheim sandstones. These experiments produced compaction bands consistently intersect the pre-existing fault. To gain better mechanical understanding of the observed band geometry, we also carried out three-dimensional (3D) numerical simulations with the input elastic moduli and yield strength well-constrained from the deformation experiments. We demonstrated that the formation of deformation bands is dictated by stress concentrations associated with the pre-existing fault. Frictional slip along the heterogeneous fault plane can produce a local stress concentration that would be responsible for further localized damage and the development of deformation zones. When fault slip is restricted (a possible result of high confinement), compaction bands initiate at high stress concentration sites resulting from geometrical irregularities of the fault. Finally, using a plane-strain two-dimensional (2D) linear-elastic model with the geometry of the faults mapped in the outcrop, we were able to provide a mechanical explanation of the distribution for deformation bands observed at the Makhtesh Katan study area.

1. Introduction

Faults in porous sandstone commonly develop in several stages. Initially, strain is accommodated by the formation of single deformation bands, which are millimeters to centimeters thick tabular zones of deformation (Aydin, 1978; Aydin and Johnson, 1978; Aydin and Johnson, 1983; Weinberger et al., 1995; Weinberger et al., 2000; Katz et al., 2004; Schultz and Siddharthan, 2005; Avdin et al., 2006; Fossen, 2010). Deformation bands commonly show a change in porosity, permeability and average grain size in comparison to their host rock (Fossen et al., 2007). Deformation bands that show a decrease in porosity also tend to be more cohesive than their surroundings, making them more resistant to weathering (Aydin, 1978). In a more advanced stage of faulting, a zone of deformation bands is formed. It consists of at least two closely spaced sub-parallel deformation bands that can reach a width of up to several decimeters (Aydin and Johnson, 1978). Finally, dense zones of deformation bands may develop one or more slip surfaces that are discrete, locally planar surfaces of discontinuity. The slip surfaces may accommodate large amounts of displacement (meters and more). They

can often be distinguished by striations and grooves along the planar discontinuity.

Deformation bands may be categorized using a kinematic-based framework, which relates to the type of deformation constricted in tabular zones (Aydin et al., 2006): (a) volumetric deformation bands with no shear offset, including compaction (pore volume reduction) and dilation (pore volume increase) bands, and (b) shear bands, including simple shear bands (also known as isochoric shear bands), compactional shear bands and dilational shear bands, of which the latter two are shear bands that underwent some volumetric change. Deformation bands, and particularly compaction bands, often lead to considerable anisotropic permeability reduction (e.g., Zhu et al., 2002, 2007; Vajdova et al., 2004) and their formation has also been linked to borehole breakouts (Haimson, 2007; Dresen et al., 2010). Hence, better understanding of the development of compaction bands has important implications in fault mechanics as well as oil and gas exploration.

Our understanding of the formation mechanisms of compaction bands observed in the field is incomplete. It is generally agreed that compaction bands form under moderate to high confining pressures

E-mail address: hannah.rubin@mail.huji.ac.il (H. Gajst).

^{*} Corresponding author.

H. Gajst et al. Tectonophysics 747–748 (2018) 1–15

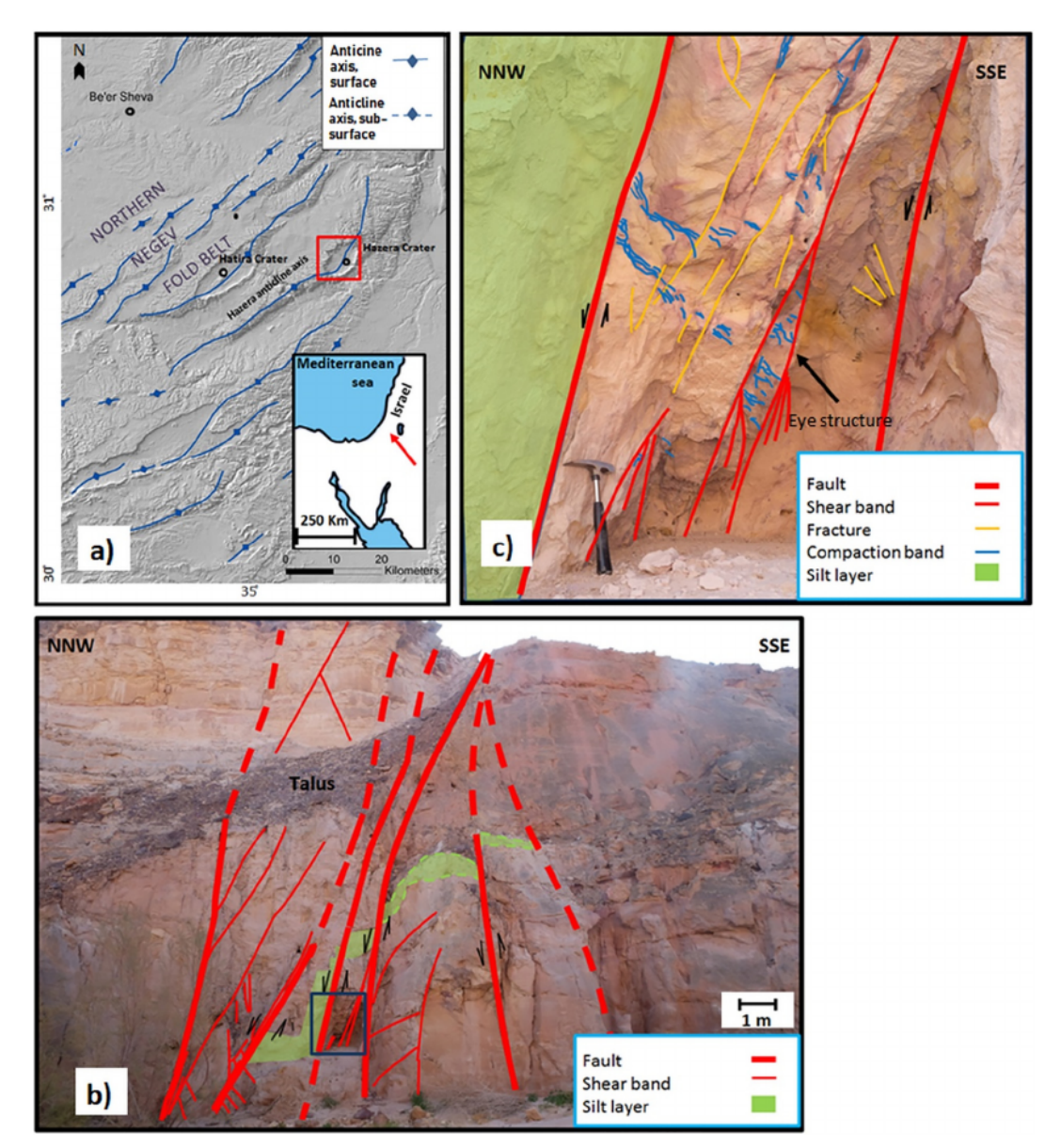


Fig. 1. (a) Location map and the geologic setting of the study area after Sneh and Weinberger (2014). Solid lines show the trends of the 'Syrian Arc' anticline axes. The study area is marked by a box. (b) Site 1 (30°57′01.4″N,35°12′02.5″E) - massive layers of the Hatira sandstone in Makhtesh Katan cross cut by six faults and many shear bands. A silt layer with high content of clay (marked in green) serves as a marker and indicates the amount of throw along the fault. Blue box marks the area in (c). (c) Close view of the deformation zone in between two faults (thick red lines) showing shear bands (thin red lines) and a delicate mesh of a few mm thick and several cm long compaction bands with wavy geometry (blue lines). Open fractures (orange lines) are commonly oriented parallel to the faults and appear to be later structures connected to the exposure and weathering of the outcrop. Geologic hammer is 30 cm long. (For interpretation of the references to color in this figure legend, the reader is referred to the web version of this article.)

(Wong et al., 2001; Fortin et al., 2006; Fossen et al., 2011). Although it is known that compaction bands commonly form in porous rocks (Fossen et al., 2011), high porosity does not assure the formation of compaction bands (Deng and Aydin, 2012). Laboratory investigations show that the formation of compaction bands is often dictated by confining pressures (Wong et al., 2001; Fortin et al., 2006; Fossen et al., 2011). In general, porous sandstones fail by shear bands or compactional shear bands at low confinements, and by diffused cataclastic flow at high confinements (e.g., Lyakhovsky et al., 2015). Baud et al. (2004) demonstrated that compaction bands form at intermediate confinements. There is a discrepancy between the stress required to generate

. .

homogeneity of the outcrop etc., also play a role in compaction-band formation

In the field, deformation bands are often juxtaposed with faults. To date, the relationship between pre-existing faults and the formation of compaction bands is not well understood. The evolution of deformation bands, i.e., the effect of existing deformation band's geometry, kinematics and physical properties on the development of new deformation bands has yet to be systematically studied.

This study reports on the geometric relation between compaction bands, shear bands and faults in Lower Cretaceous porous sandstone at Makhtesh Katan, Israel. To understand the field observations, we con-

H. Gajst et al. Tectonophysics 747–748 (2018) 1–15

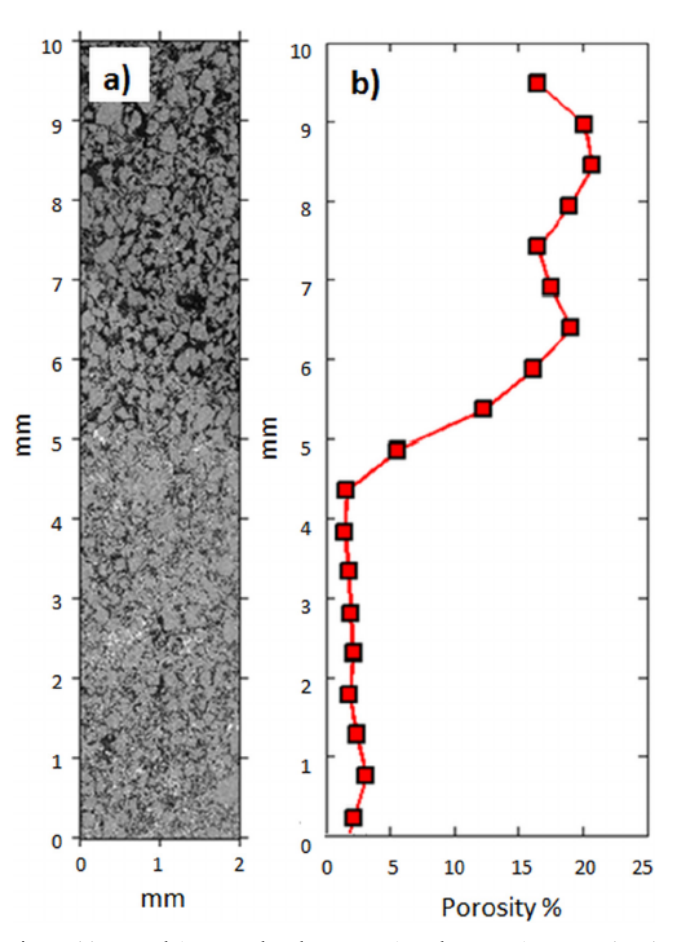


Fig. 2. (a) Merged images taken by a scanning electron microscope (SEM) showing a representative compaction band (blue lines on Fig. 1c) within the porous Hatira sandstone. Quartz grains and pores appear in gray and black, respectively. The pores in the compacted area are partially filled with iron-rich precipitates, which appear as white dots. (b) Variations of 2D porosity (%) across the 10 mm section in 2a. The porosity declines gradually from values of ~15%–20% between 10 and 6 mm to values < 3% between 4 and 0 mm. The latter values represent the closely packed compaction bands.

formation by generating local stress concentrations and provide new mechanical understanding of the formation of compaction bands associated with faults. The difference in the conditions governing compaction localization has important inference on the complexity of the deformation structure of porous sandstones.

2. Field observations

Outcrops containing porous sandstone are studied at Makhtesh Katan ("Small Crater", also known as Hazera Cirque), Israel. Makhtesh Katan is an erosive crater located in the northeastern Negev (Fig. 1a). The main structural element in the study area is the Hazera anticline, a NE-SW trending monocline with steep beds dipping up to 90 $^{\circ}$ to the southeast and moderate beds dipping $\sim\!5$ $^{\circ}$ to the northwest. The monocline is about 55 km long and between 8 and 15 km wide (Eran, 1982; Shamir and Eyal, 1995). This structure is part of a series of folds composing the 'Syrian Arc' fold belts (Krenkel, 1924), which began to

1995

Several discontinuities of different scales are observed in the study area, the largest of which are faults that throw (> 130 m) the Hatira Formation against the Jurassic Zohar Formation. On a smaller scale, there are numerous faults within the Hatira Formation, which accommodate displacements of several centimeters to several meters (Fig. 1b). Around these faults there are numerous deformation bands of several millimeters to several decimeters in thickness.

We present the results from three main outcrops. The first outcrop shows at least six faults composing a fan-shaped deformation zone (Fig. 1b). Between two of these faults, we observe a set of sub-parallel shear bands and serval sets of meshes of short deformation bands that have developed at an angle of between $45^{\circ} - 70^{\circ}$ to the adjacent faults (Fig. 1c). The deformation bands composing these meshes are small, approximately millimeters thick and several centimeters long with a wavy geometry. Thin sections made from this zone show a dramatic decrease in porosity, from around 20% in the host rock to < 5% in these deformation bands (Fig. 2). Due to their resemblance to the compaction bands observed in other settings (Mollema and Antonellini, 1996; Eichhubl et al., 2010; Fossen et al., 2011) and produced in experiments (Fortin et al., 2006; Wong et al., 2001), these bands were given a field characterization of "compaction bands". Field relations suggest that the faults and most shear bands formed prior to these compaction bands, since the compaction bands terminate against the faults, yet do not seem to be displaced by them. It should be noted that the shear bands may have still been active during the formation of the compaction bands, and new ones may have still formed in other areas of the shear zone. Some compaction bands are confined between faults inside an "eye-like" structure (i.e., enclaved zone between two shear bands, marked by an arrow on Fig. 1c) with no correlating compaction bands on either side of the zone. The second outcrop consists of a deformation zone, including at least one slip surface and several parallel faults and shear bands. Another set of deformation bands, recognized as compaction bands, crosses or terminates toward the set of faults and shear bands (Fig. 3a). The angle between these two sets is between 60° and 70° (Fig. 3c). The amount of shear is negligible, as demonstrated by a deformation band crossing a stratigraphic marker without visibly displacing it (Fig. 3b). Thin sections made of both sets show a decrease of over 10% in porosity in the deformation band area (Fig. 4).

The third outcrop consists of a deformation zone that is associated with a normal fault displacing at least 10 m. The deformation zone contains shear bands as well as compaction bands that cross stratigraphic markers as well as other deformation bands without visibly displacing them (Fig. 5).

Field observations suggest that the formation of compaction bands in Makhtesh Katan are associated with pre-existing shear bands. Yet the nucleation and growth of the compaction bands cannot be inferred solely from field observations. The following sections include experimental observations and numerical modeling, which provide further insight into the mechanics of compaction band formation in the field.

3. Experimental observations

The deformation history in any natural setting can be quite complex, and the stress states of the current study's outcrops is mostly unknown. To elucidate how pre-existing faults, affect the formation of compaction bands, triaxial deformation tests were conducted. We used cylindrical Bentheim sandstone samples cored perpendicular to their beddings in a diameter of 18.4 mm and with a length of 38.1 mm (Zhu, 2007).

form during the Turonian (Reches, 1976). Makhtesh Katan is located at the top of the Hazera anticline, exposing the Lower Cretaceous Hatira Formation, which is mainly composed of porous Nubian sandstone, shale and silt layers deposited on the continent (Weissbrod, 1993). This formation is overlain by tens of meters of an Upper Cretaceous carbonate sequence (Arkin and Hamaoui, 1967; Yechieli et al., 1994; Hirsch,

With an initial porosity of 23% and an average grain size of 0.2 mm, Bentheim sandstone consists of 95% quartz, 3% kaolinite and 2% orthoclase. The relatively homogeneous porous rock is known to fail by discrete compaction bands at effective confining pressures greater than \sim 100 MPa (Klein et al., 2001).

To produce the shear fracture in the intact Bentheim sandstone,

3

H. Gajst et al. Tectonophysics 747–748 (2018) 1–15

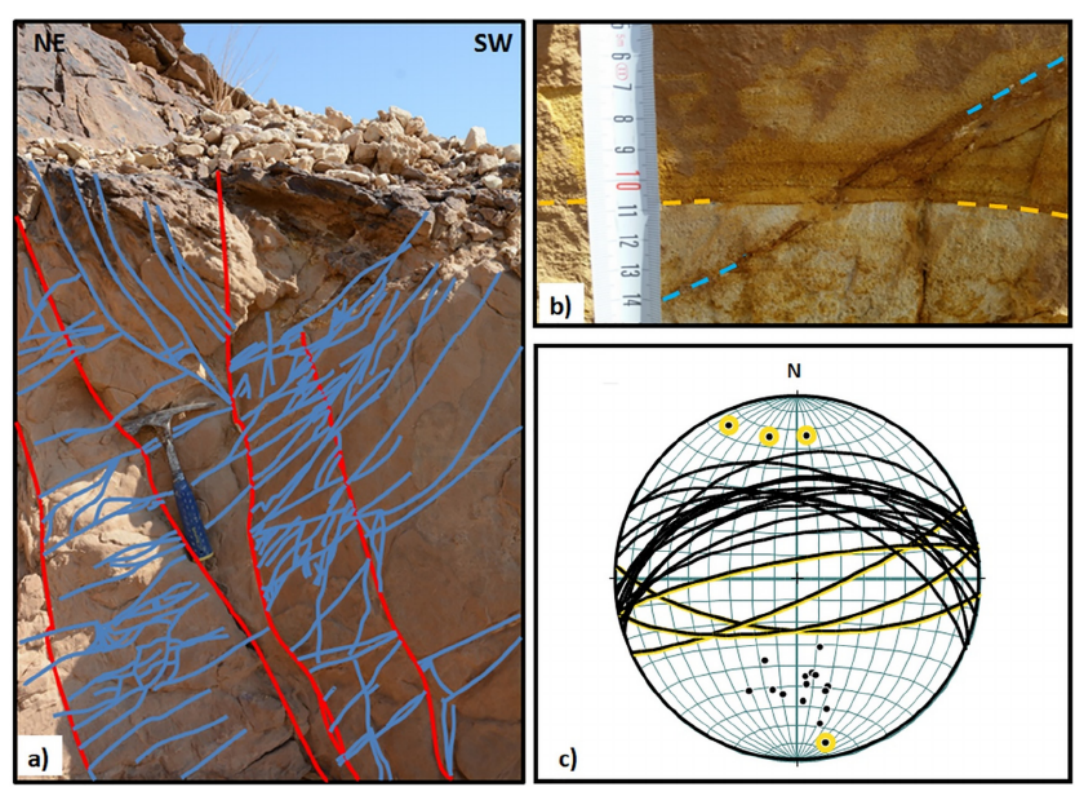


Fig. 3. (a) Site 2 (30°57′21.6″N, 35°12′05.4″E) - an outcrop showing several parallel faults, shear bands (red lines) and compaction bands (blue lines) with mutual cross-cutting relations. Geologic hammer is 30 cm long. (b) A deformation band (dash blue line) crossing a stratigraphic marker (dash orange line) 1 m away from the deformation zone shown in Fig. 2a. The stratigraphic marker is not displaced by the compaction band. (c) Lower-hemisphere, equal-area projections of fault (marked with yellow) and compaction band (marked with black) orientations collected from the outcrop shown in Fig. 2a: the average angle between the two sets is about 60°–70°. Pen is 14 cm long. (For interpretation of the references to color in this figure legend, the reader is referred to the web version of this article.)

oven-dried samples were first loaded to failure, deformed at an effective pressure of 5 MPa and at a constant strain rate of 1.3e $^{-5}$ 1/s. The maximum principal stress, σ_1 , was parallel to the main axis of the cylindrical sample. Once the shear strength was exceeded, the axial load was removed immediately to avoid any slip along the shear fracture. Visual examination confirmed a through-going shear fracture at $\sim\!30\,^{\circ}$ relative to σ_1 .

The pre-faulted samples were then saturated in distilled water, jacketed and loaded into the deformation apparatus again, where they were deformed at various confining pressures (15 MPa, 60 MPa, 110 MPa, 160 MPa and 210 MPa) at the same constant strain rate as the first stage. A constant pore pressure of 10 MPa was maintained during the deformation tests, so that the effective pressures (confining pressure – pore pressure) in these experiments were 5, 50, 100, 150, and 200 MPa.

The yield stress in the pre-faulted Bentheim sandstone samples was marked by a surge in acoustic emissions (Fig. 6). Fig. 7a shows the yield stresses of the pre-faulted Bentheim samples plotted against the compactive yield cap corresponding to the onset of shear-enhanced compaction C* for intact dry samples (Klein et al., 2001), as well as the compactive yield stresses of circumferentially notched dry samples

. .

. .. .

1 00000 -

different extents of grain crushing were visible in the optical micrograph (Fig. 8). In some areas grain crushing was so severe that the fragmented grains could be detected only by SEM imaging (Fig. 8d). In contrast, other areas along the fault showed little to no grain damage and were hard to distinguish from the rest of the sample away from the pre-existing fault (Fig. 8b).

With the increasing effective confining pressure, the post-yield deformation exhibited diffuse to discrete compaction localization. At 50 MPa, an area with intense grain crushing could be spotted initiating from the pre-existing fault (Fig. 9). This area showed porosity reduction but could not be described as a discreet compaction band due to its diffused nature. Nevertheless, it could be recognized as a diffused compaction band, similar to structures produced in experiments by Baud et al. (2004). At 100 MPa, a discreet wavy compaction band perpendicular to σ_1 formed far from the edges of the sample (Fig. 10). At 150 MPa, a series of compaction bands formed close to the sample's edge. They appeared to initiate at the pre-existing fault (Fig. 11). No compaction bands developed in the center of the sample. At 200 MPa, a series of wavy compaction bands developed close to one edge of the sample, crossing the pre-existing fault. These bands were generally perpendicular to σ_1 . Close to the second edge of the sample, an area that

. .

.

. .

(Tembe et al., 2006). It was snown that, similarly to the notched samples, the pre-faulted samples yielded at stresses lower than the intact samples.

Deformed samples were retrieved and halved along the axial direction. Double polished thin sections $30\,\mu m$ thick were prepared. Microstructural analyses were conducted using both optical and scanning electron microscopes (SEM).

The post-yield behaviors varied considerably at different effective confinements. In the sample deformed at 5 MPa, the post-yield damage concentrated along the pre-existing fault. Along the fault, patches with

underwent severe grain crushing and porosity reduction could be spotted and was associated with a large deformed concentration of kaolinite. Close to the center of the sample, a well-defined wavy compaction band developed between the circumference of the sample and a curve in the pre-existing fault, perpendicular to σ_1 (Fig. 12).

The experiment with an effective confining pressure of 200 MPa showed a clear connection between a geometrical anomaly of the pre-existing fault (Fig. 12) and the formation of a well-defined compaction band. The 150 MPa experiment was done on a sample that had a pre-existing planer fault, lacking geometrical anomalies, and did not

4

H. Gajst et al. Tectonophysics 747–748 (2018) 1–15

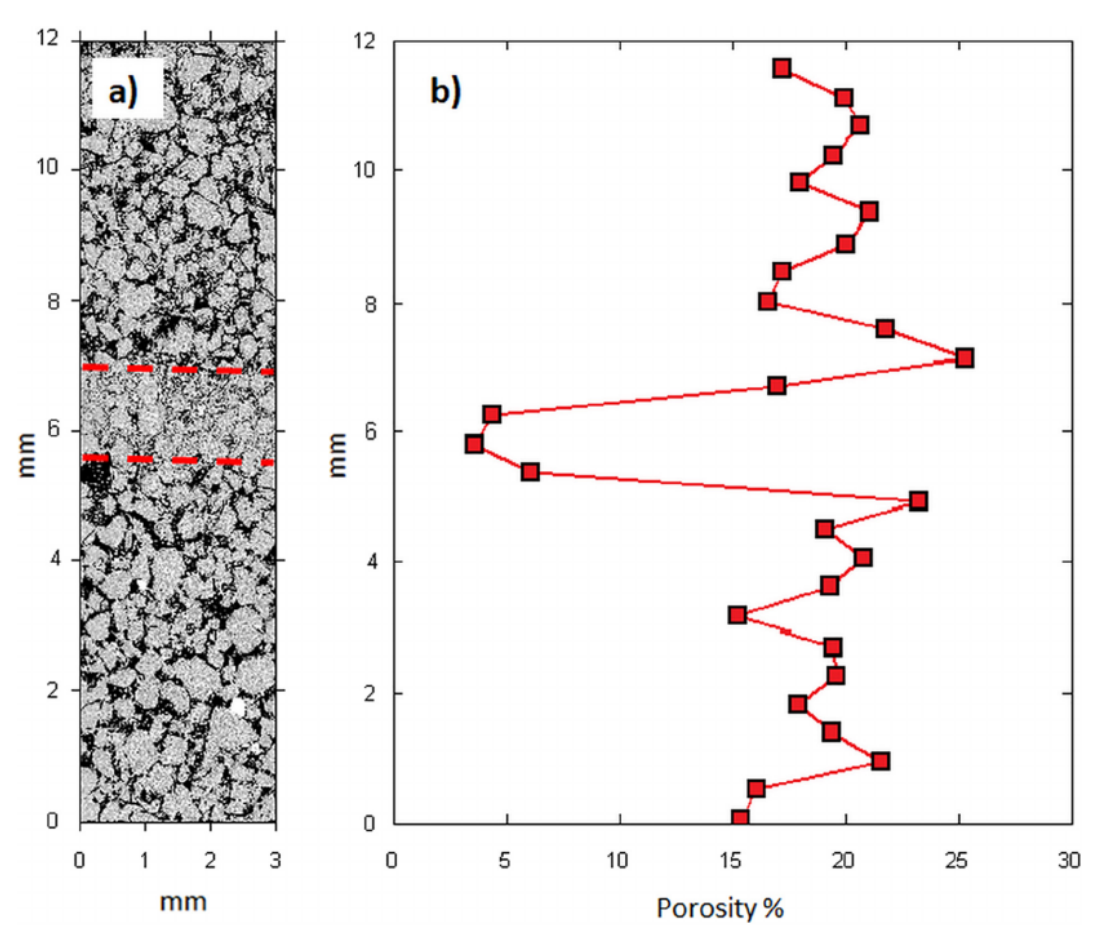


Fig. 4. (a) Merged images taken by a scanning electron microscope (SEM) showing a representative compaction band (blue lines on Fig. 3a) within the porous Hatira sandstone. Quartz grains and pores appear in gray and black, respectively. The pores in the compacted area, in between the two dashed red lines, are partially filled with iron-rich precipitates, which appear as white dots. (b) Variations of 2D porosity (%) across the 10 mm section in 3a. The porosity declines gradually from values of \sim 15%–20% to values < 3% at the compacted area. The latter values represent the closely packed compaction bands. (For interpretation of the references to color in this figure legend, the reader is referred to the web version of this article.)

produce a compaction band in the center of the sample (Fig. 11). Yet, at 100 MPa, a similar sample containing a planer fault produced a well-defined compaction band (Fig. 10), and at 50 MPa a sample with a planer fault produced a diffused compaction band (Fig. 9). This points to the possibility that the pre-existing faults induced the formation of compaction bands by different mechanisms at higher and lower confining pressures. In the next section, we examine the different mechanisms for the formation of compaction bands induced by pre-existing faults using numerical modeling.

4. Numerical modeling

4.1. Model of experiments

the top and bottom boundaries and free boundary at the envelop of the cylinder. We simulated two case studies: (1) a planer 1 mm wide fault with a kink examining the effect of the fault's geometrical anomaly on the development of initial failure and (2) a planar, 1 mm wide, discontinuous fault representing a fault with patches of varying material properties. In general, the mechanical properties of fault rocks are considerably different from those of the wall rocks. Since the fault zones already accumulated certain amount of slip, we assumed that the material inside the fault zone had different elastic properties than their surroundings. We analyzed two cases, a 30% higher (stiff fault) and a 30% lower (soft fault) shear modulus relative to the surrounding material. It was assumed that the bulk modulus is weakly affected by the accumulated slip and remained constant throughout the volume of the

The connection between faulting and the development of compaction localization in our experiments was studied by a 3D linear-elastic numerical simulation using COMSOL Multiphysics software (COMSOL AB, 2006). We simulated pre-faulted Bentheim sandstone cylinders, deformed under constant confining pressures (50, 100, 150 and 200 MPa). We used a superposition of the solution for hydrostatic loading and uniaxial loading with displacement boundary conditions at

simulated cylinders. The surrounding simulated rock had a shear modulus of 4.7 GPa and Poisson ratio of 0.15. The simulations were halted when the first element failed (reached the yield cap) outside the fault.

In all simulations, the first element to fail was in contact or in very close vicinity to the fault (Figs. 13, 14). The average *Q-P* values $\left(Q = \sigma_1 - \sigma_3; P = \frac{(\sigma_1 + \sigma_2 + \sigma_3)}{3}\right)$ of the top boundary of the simulated samples are plotted in Fig. 7b. These values represent the average

5

H. Gajst et al. Tectonophysics 747–748 (2018) 1–15

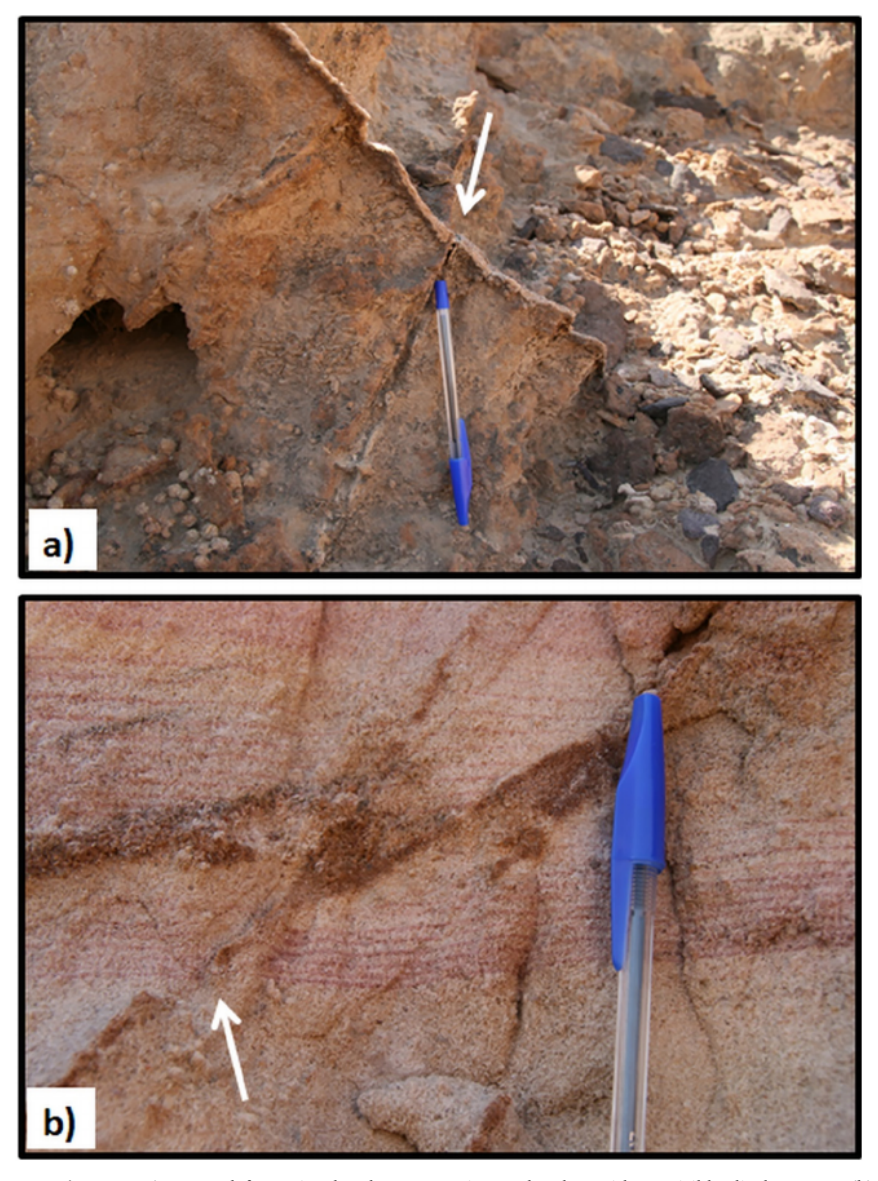


Fig. 5. (a) Site 3 (30°57′33.5″N, 35°12′06.8″E) - Two deformation bands cross-cutting each other with no visible displacement. (b) Site 3 - A compaction band crossing stratigraphic markers with no visible displacement. Cross-cutting locations are indicated by arrows.

stresses of the sample, similar to the values measured by sensors in laboratory experiments. These values can be compared to the yield existing fault in the 200 MPa experiment, whether the fault was soft or stiff (Fig. 13a, b). At the lower stresses (50 and 100 MPa) it failed on the

values found in the triaxial tests, marked as hollow gray squares in Fig. 7a. They are mostly under the yield cap, and similar to the results of the experiments presented in the previous section. The stress states of the first elements to fail in each simulation were also marked on a Q-P diagram, presented in Fig. 7c. We analyzed the $\Delta\sigma_{YC}$ which is the stress difference on a Q-P diagram between the stress state and the yield cap, near a fault kink with a similar angle to that of the fault in the 200 MPa experiment (Fig. 12). The results showed that, at 200 MPa and 150 MPa, the simulated sample failed on the same side of the kink as the compaction band observed propagating from a curve in the pre-

same side when the fault was stiff, and on the opposite side when the fault was soft (Fig. $13c,\,d).$

The simulations with a discontinuous fault failed differently at higher and lower stresses. At 200 and 150 MPa, the initial failure points were at the sides of the faults (Fig. 14a, b). At lower stresses (50 and 100 MPa) and with stiff faults, the failure points were at the sides of the fault (Fig. 14d). For lower stresses and soft faults, the failure points were at the fault tips, propagating the tips one toward the other (Fig. 14c).

Our simulations reproduced failure under a large range of confining

6

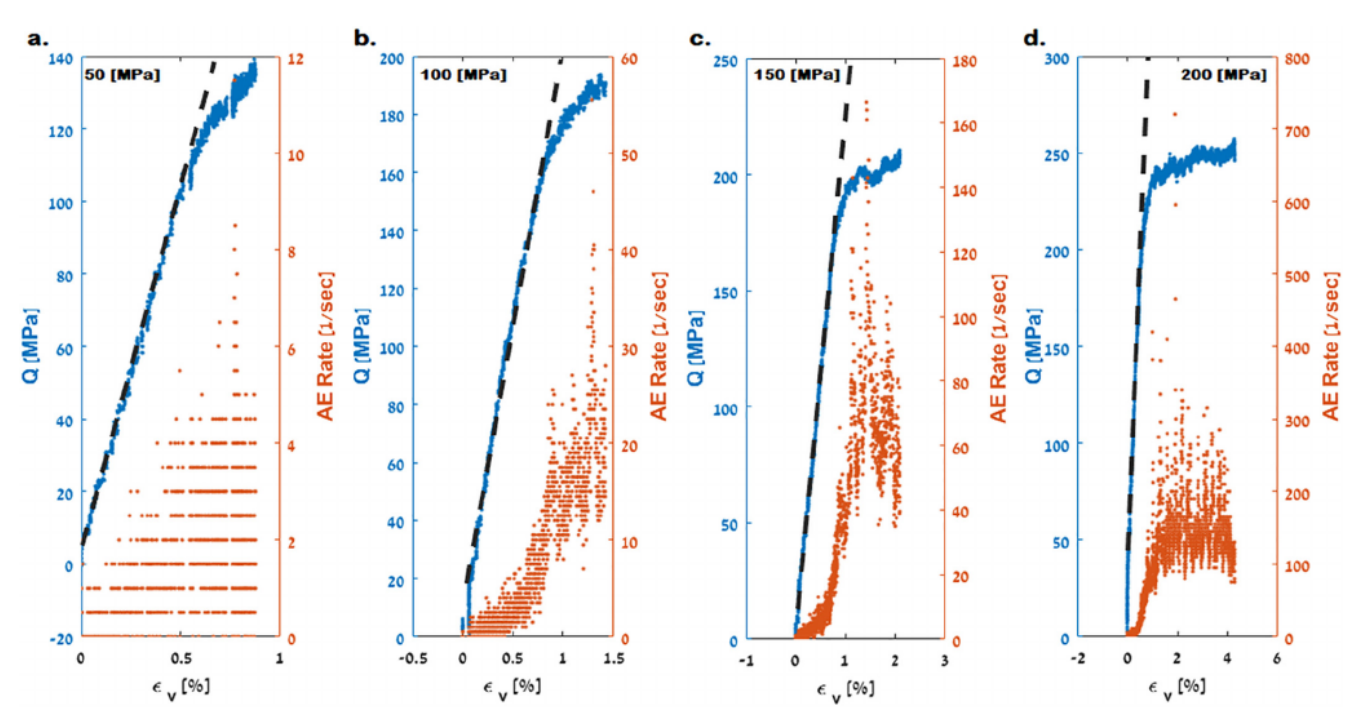
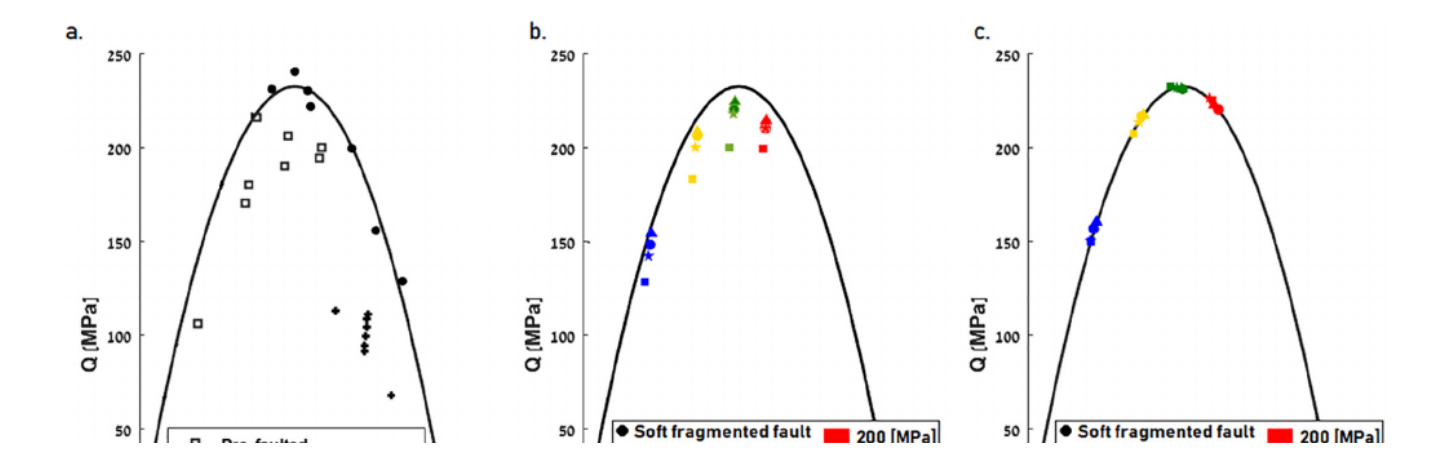


Fig. 6. (a)—(d) Differential stress (blue) and AE rate (red) verses volumetric strain for experiments done on pre-faulted Bentheim samples at different effective pressures of 50, 100, 150 and 200 MPa. Dashed lines mark the initial linear-elastic behavior of the sample before yielding. (For interpretation of the references to color in this figure legend, the reader is referred to the web version of this article.)



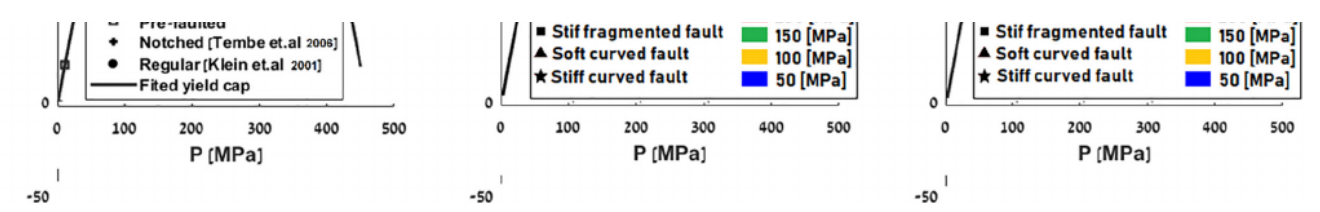
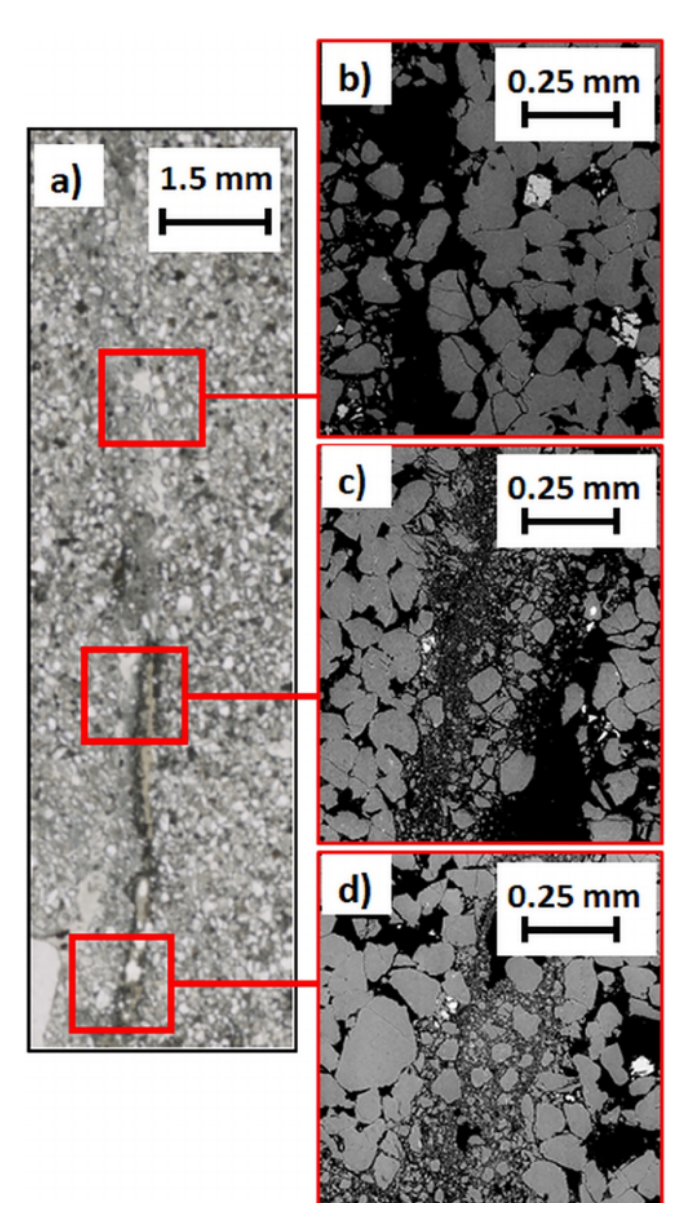


Fig. 7. (a)—(c) Differential stress versus mean stress (*Q-P* diagrams). (a) Pre-faulted failure points (gray open squares) plotted along with results from previous studies. These studies included triaxial experiments with whole (solid circles; Klein et al., 2001) and notched (pluses; Tembe et al., 2006) Bentheim sandstone samples. A yield cap fitted to the results of Klein et al. (2001) is marked by a black line. (b) Results of 3D triaxial simulations of pre-faulted samples with different fault geometries and properties and various effective pressures. (c) The same as b, with markers showing the stress at the points of initial yield.

7

H. Gajst et al. Tectonophysics 747–748 (2018) 1–15



4.2. Model of field outcrop

In order to better understand the role played by pre-existing faults in the formation of compaction localization observed in the field (Fig. 1), we built a plane-strain 2D linear-elastic numerical model, using COMSOL Multiphysics software (COMSOL AB, 2006). The model contained the geometry of the faults mapped in the Site 1 outcrop (fault boundaries are marked by black lines on Fig. 15.) Displacement boundary conditions of different magnitudes were applied at a distance of 25 m in each direction, parallel to the main faults (direction of the displacement is marked by arrows on orange boundaries in Fig. 15), allowing the first points in the outcrop to fail. The top and bottom boundaries were free (marked in green in Fig. 15). We assumed a lithostatic stress of 14.5 MPa, calculated according to the weight of the stratigraphic column above the Hatira Formation at the postulated time of deformation (the end of the Turonian age).

Similar to the rock sample modeling discussed above, we prescribed different elastic properties for the material within the fault zone and for the surrounding rock. The shear modulus of the surrounding rock was adopted as 4.7 GPa and Poisson ratio was 0.15. The shear modulus of the fault zone was reduced by up to 90% relative to the surrounding rock, this is understandable because the amount of slip along the laboratory faults is usually small, whereas the cumulative slip along natural faults can be larger by magnitudes. We excluded one fault that according to our simulations was formed at a later stage. It was also assumed that the bulk modulus is weakly affected by the accumulated slip and remained constant throughout the outcrop. This seemed appropriate since we are not interested in the stress developing inside the fault zones but only in the stress field surrounding them.

Since the non-deformed sandstone in the outcrop was too fragile to perform triaxial tests, we used an estimated yield cap, shown in Fig. 16, to determine failure points. The yield cap was chosen as a parabolic function converging to the left of its maxima, with a line representing the Coulomb-Mohr failure criterion with an internal friction angle of $\mu=0.6$. The hight of the yield cap was tested using the stress results of the numerical model to satisfy conditions at high stress locations within the model (marked as red points A–E in Fig. 15). A *Q-P* diagram (Fig. 16) shows a fan of black lines marking the deformation path of the five observation points (shown in Fig. 15) placed at the highest stress concentration. Fig. 16 also shows a green line marking the deformation path of an observation point placed at a distance from the faults (marked as green point F on Fig. 15), representing the average stress conditions of the outcrop. In this simulation, the displacement magni-



Fig. 8. (a) Scanned image of a fault obtained from the sample that deformed under an effective pressure of 5 MPa. Red squares mark the areas enhanced in b–d. (b) SEM image showing almost no damage to the grains and minor porosity reduction. (c) Extensive grain crushing and porosity reduction. No large grains are observed in the matrix. (d) Extensive grain crushing and porosity reduction. Large and unbroken grains are observed in the matrix. (For interpretation of the references to color in this figure legend, the reader is referred to the web version of this article.)

pressures, similar to the results seen in our experiments. The simulation results suggest that both geometrical anomalies and discontinuities of faults induce sufficient stress concentrations to allow the nucleation of a compaction band in the center of the sample. The progression of these bands to their final appearance was not modeled.

tude at the boundary was incrementally increased up to 3.2 cm. Markers of different colors along the deformation paths represent simulations with varying displacements along the boundaries. The figure also contains a set of five possible yield caps. #3 (marked in red) is the optimal yield cap, chosen because a higher yield cap's maximum would result in dilation and a lower yield cap's maximum would result in failure of the host rock.

Fig. 17 shows the spatial distribution of the $\Delta\sigma_{Yo}$ which is the stress difference in a *Q-P* diagram between the stress state and the yield cap. Negative values refer to a distance below the yield cap. Areas where compaction bands formed in Site 1 are marked as dotted black lines.

Points A, B, C, and D (Fig. 17) are located in the areas that failed first. Indeed, these are the areas where compaction bands were found. The mode of failure at points A, B, and C is compatible with compaction bands, because these points fail around the yield cap maximum. The results of the model could only partially be examined using strain localization analysis suggested by Issen and Rudnicki (2000). We could

8

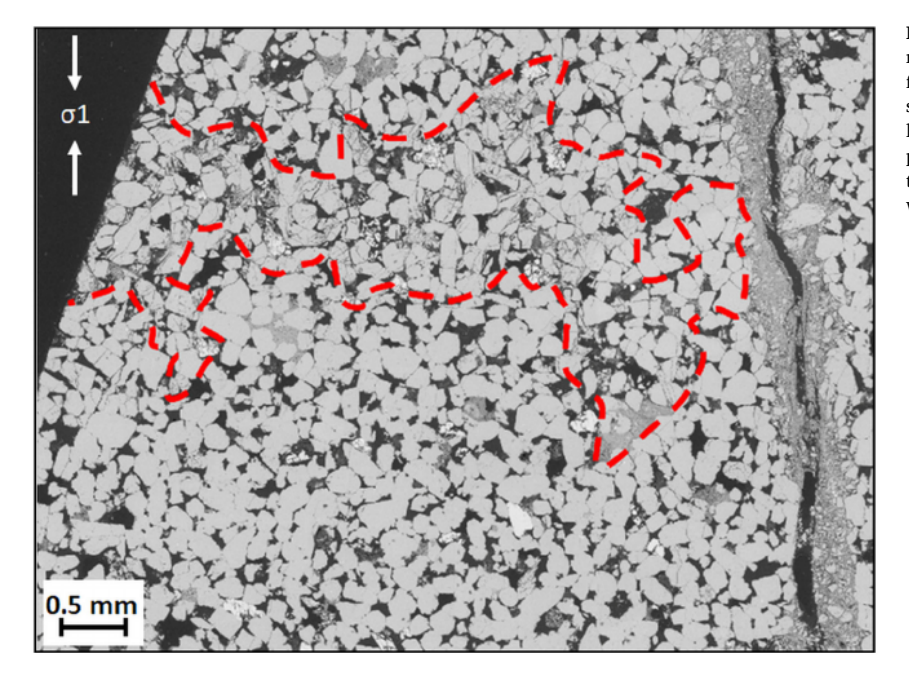


Fig. 9. (a) A composite of SEM images of the area surrounding the fault in the sample deformed under an effective pressure of 50 MPa. An area of grain crushing and slight reduction of porosity consistent with compaction localization (dash red line) is observed and appears to be perpendicular to σ_1 . (For interpretation of the references to color in this figure legend, the reader is referred to the web version of this article.)

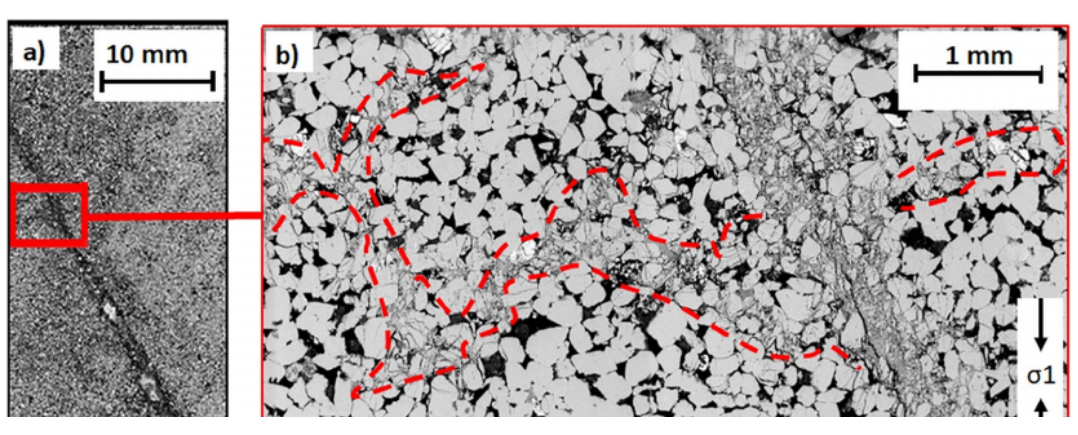




Fig. 10. (a) Scanned thin section of the sample that deformed under an effective pressure of 100 MPa. (b) SEM image of the marked area in (a), showing a discrete compaction band with wavy geometry (dash red line) that formed perpendicular to σ_1 . (For interpretation of the references to color in this figure legend, the reader is referred to the web version of this article.)

not check the yield cap of the outcrop sandstone, and do not know what flow rule would be appropriate after yield. Our calculations showed that, assuming a dilation coefficient value smaller than -2.5, the bands were predicted to be perpendicular to σ_1 . This kind of elastic modeling only simulates the origin of compaction bands. The progression of these bands to their final appearance was not modeled.

5. Discussion and conclusions

5.1. Geometry of compaction bands and associated stress field

The appearance and identification of compaction bands in the

Hazera anticline, Israel, are discussed in the light of several types of compaction bands that have been previously observed in the field and characterized by their geometry and scale. Wavy, chevron, and straight compaction bands were reported in Buckskin Gulch, Utah, and the Valley of Fire State Park, Nevada (Mollema and Antonellini, 1996; Aydin and Ahmadov, 2009). Later work by Eichhubl et al. (2010) indicated that only one of the compaction band populations at the Valley of Fire could be categorized as *pure compaction bands* (with no indication of shear offset), while the rest of the populations were categorized as *shear enhanced compaction bands*, which are highly compactional bands with a shear component that is less than a tenth of their width. Fossen et al. (2011) also re-categorized the straight compaction band

9

H. Gajst et al.

Tectonophysics 747-748 (2018) 1-15

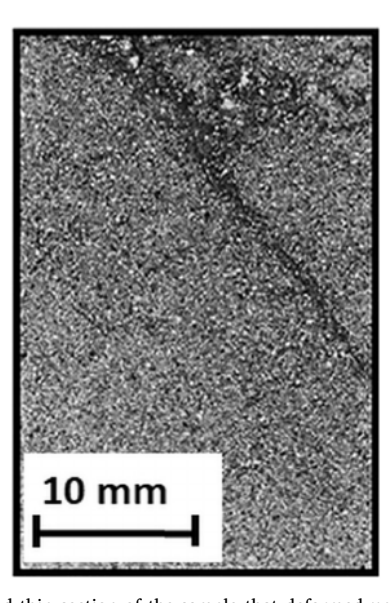


Fig. 11. Scanned thin section of the sample that deformed under an effective pressure of 150 MPa.

population at Buckskin Gulch as shear enhanced compaction bands. In addition, Ballas et al. (2013) described conjugate sets of shear enhanced compaction bands found in the Rhône Valley, France. The geometry of the pure compaction bands was almost always wavy – similar to the geometry of the compaction bands found at Site 1 (Fig. 1c). In contrast, shear enhanced compaction bands were either planar or chevron, similar to the planar geometry of the compaction bands found in Sites 2 and 3 (Fig. 3a, b and 4).

There has been some previous discussion regarding the relation between various types of compaction bands found in the field and the shear zones, while in Sites 1 and 2 there was a clear indication that the faults induced the formation of the compaction bands.

5.2. Discrepancies between laboratory and field observations

The minimal effective pressure required to experimentally produce compaction bands in different types of sandstone ranges between 60 and 200 MPa (Wong et al., 2001; Baud et al., 2004; Fortin et al., 2006). These effective pressures are higher than those estimated in the field (Fortin et al., 2006; Fossen et al., 2011), and much higher than the estimated effective pressures experienced by the outcrops discussed in the current study, that are estimated between 10 MPa and 20 MPa. The present experiments in varying confining pressures showed that nucleation of compaction bands may also be enhanced due to the presence of pre-existing faults (Figs. 9-12). Fortin et al. (2006) also noted that compaction bands produced in experiments showed a larger amount of grain crushing and damage than seen in previous field studies, attributing the difference to extensive healing processes and low strain rates in nature. Thin sections of compaction bands made in our study also showed extensive grain crushing and grain size reduction comparable to the changes seen in experiments.

Previous experiments in Bentheim sandstone were able to produce pure compaction bands in whole samples at effective pressures higher than 120 MPa (Baud et al., 2006). The results were reported to be similar in dry and drained conditions. Typically, compaction bands formed at the top and bottom edges of the sample perpendicular to σ_1 , while new bands propagated inwards. The formation of compaction bands at effective pressures as low as 90 MPa were previously reported, but only in samples that also developed high angled shear bands (Baud et al., 2006). Our experiment showed that the presence of a pre-existing fault was associated with the formation of a diffused compaction band at an effective pressure as low as 50 MPa. We also showed that the presence of pre-existing faults affected the location of the compaction bands, namely, at effective pressures of 200 MPa and 100 MPa, our experiments formed discreet compaction bands at the center of the samples. Charalampidou et al. (2017) also showed that a pre-existing

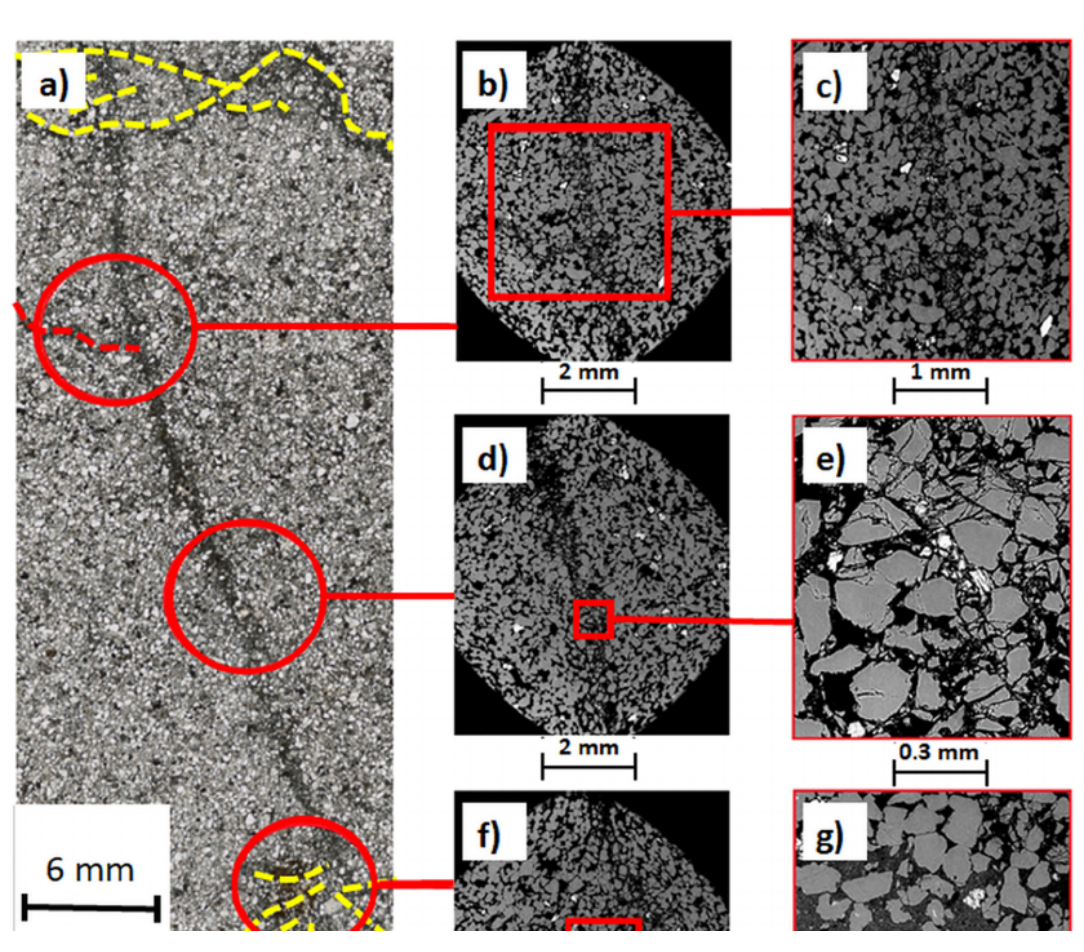
local stress regime: Mollema and Antonellini (1996) suggested that compaction bands formed at the compactional quadrants of shear bands. The orientation variations among the compaction band populations led Aydin and Ahmadov (2009) to suggest that either some of the compaction bands did not coincide with the principal stress, or else they were formed under a highly anisotropic and heterogeneous stress field. Later studies suggested that both at the Valley of Fire and Buckskin Gulch pure compaction bands were perpendicular to the regional σ_1 direction, while the shear enhanced compaction bands formed a high angle conjugate set of about 70° – 75° , linking their formation to the local stress regime (Fossen et al., 2011; Fossen et al., 2015). In contrast, in this study the pure compaction bands in Site 1 are very short structures that appear to have been formed as a result of stress induced by the activity of pre-existing faults and shear bands, and not directly by the regional stress regime. The mechanical simulations of this outcrop show that the geometry of pre-existing faults and shear bands within the outcrop induces the stress concentration that facilitates the nucleation of the compaction bands (Fig. 13). At Site 2, shear enhanced compaction bands formed at a high angle to pre-existing faults and shear bands, crossing them with no apparent displacement (Fig. 3a). In Site 3, shear enhanced compaction bands formed as parts of a complex system of deformation bands composing a deformation zone of a relatively large fault (Fig. 4). In all three sites, the compaction bands were linked to

fault may induce the development of a compaction band at the center of a Bentheim sample under an effective pressure of 185 MPa.

5.3. Mechanisms of interaction between faults and compaction bands

Our field observations and lab experiments showed a clear relation between the presence of pre-existing faults or shear bands and the formation of compaction bands. This was also supported by numerical modeling. Previous studies have shown that local variations in deformation band distribution and clustering patterns can be linked to dune boundaries (Mollema and Antonellini, 1996; Eichhubl et al., 2010; Fossen et al., 2011), slight changes in lithology, such as change in clay mineral content (Mollema and Antonellini, 1996), changes in sandstone porosity (Fossen et al., 2011) and geometrical abnormalities (Nicol et al., 2013). Thus, it appears that, although on a large-scale deformation band networks are affected by the regional tectonic regime (Soliva et al., 2016), on a smaller scale, shear band network patterns are highly sensitive to local stress changes of various sources. This fits our field observations and numerical results regarding Site 1, linking the formation of locally distributed mesh of compaction bands to stress concentration induced by pre-existing faulting. This also fits our experimental results, that showed that stress concentrations induced in pre-faulted samples allowed the formation of compaction bands in the

10





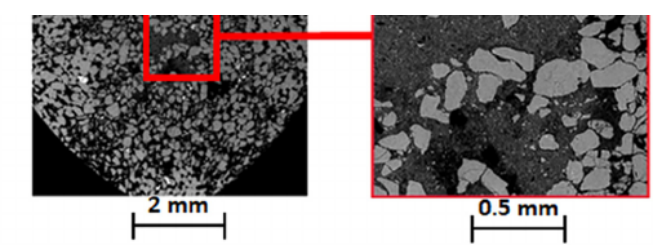


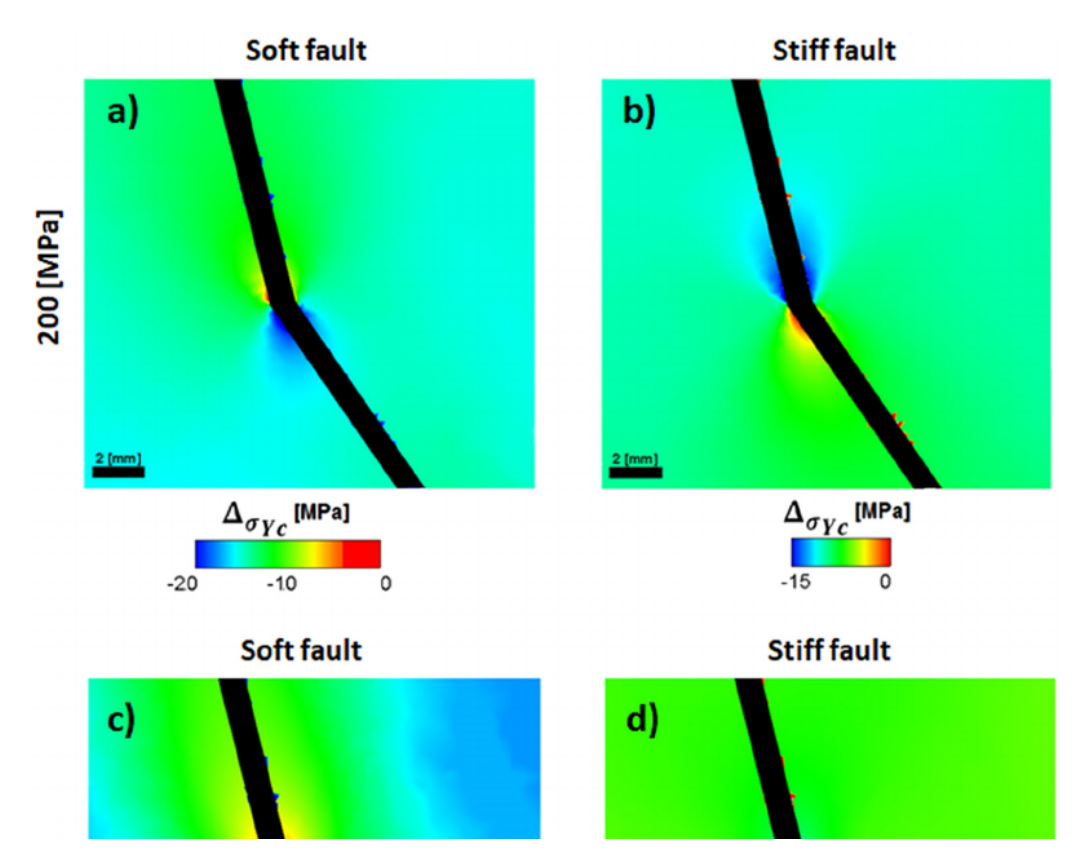
Fig. 12. (a) SEM image of a deformed sample under an effective pressure of 200 MPa. Compaction bands formed close to the sample's upper and lower edges (dashed yellow lines), as well as at the center of the sample (dashed red line) that are perpendicular to σ_1 . Red circles mark enhanced areas in b, d, and f. (b) The intersection between the central compaction band and the fault. Note the wavy geometry of the compaction band. (c) Close-up of the marked area on Fig. 12b, showing no visible microscopic difference between the damage accumulated by grains in the compaction band and the fault. (d) Close-up of the pre-existing fault. (e) Close-up of the marked area on Fig. 12d, showing damage accumulated by grains. The grains in the figure are severely crushed but their original shape can be reconstructed. (f) Compaction localization and compaction bands close to the lower boundary of the sample. The damage appears to concentrate around an area with a high concentration of deformed kaolinite. (g) Close-up of the marked area on Fig. 12f, showing quartz grains surrounding an area of deformed kaolinite. (For interpretation of the references to color in this figure legend, the reader is referred to the web version of this article.)

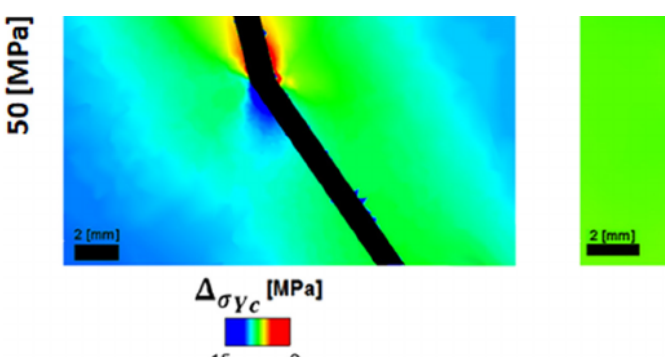
center of the samples, and not only at the top and the bottom of the cylinders.

It has been suggested that strain hardening of deformation bands due to either porosity loss and cataclasis (Schultz and Siddharthan, 2005) or fault locking as a result of non-planar/interfering slip surfaces (Fossen et al., 2007) may induce local stress concentrations. Connecting the evolution of the frictional properties (for instance asperity size and

distribution) of the pre-existing fault to the change in porosity, grain size and grain shape, which are not homogenous along the fault (as seen in Fig. 8) can explain the creation of stress concentrations, that may develop into compaction band nucleation sites, along it. In experiments, we would expect this mechanism to be prominent under relatively low effective pressures (< 100 MPa), that allow easier movement along the fault, thus explaining the formation of compaction bands seen in our 50

11





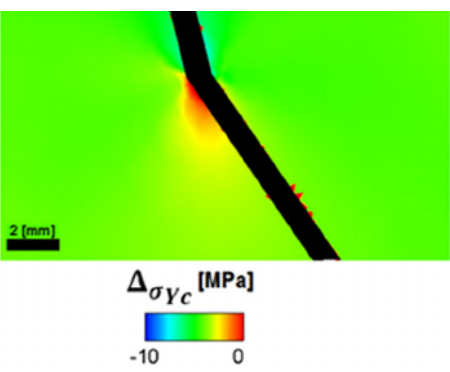


Fig. 13. Cross sections of cylinders showing $\Delta \sigma_{Yc}$ (the stress difference in a *Q-P* diagram between the stress state and the yield cap) calculated by a 3D COMSOL simulation of an axially deformed pre-faulted sandstone. (a) A stiff fault at a confining pressure of 200 MPa. (b) A soft fault at a confining pressure of 50 MPa. (c) A stiff fault at a confining pressure of 200 MPa. (d) A soft fault at a confining pressure of 50 MPa.

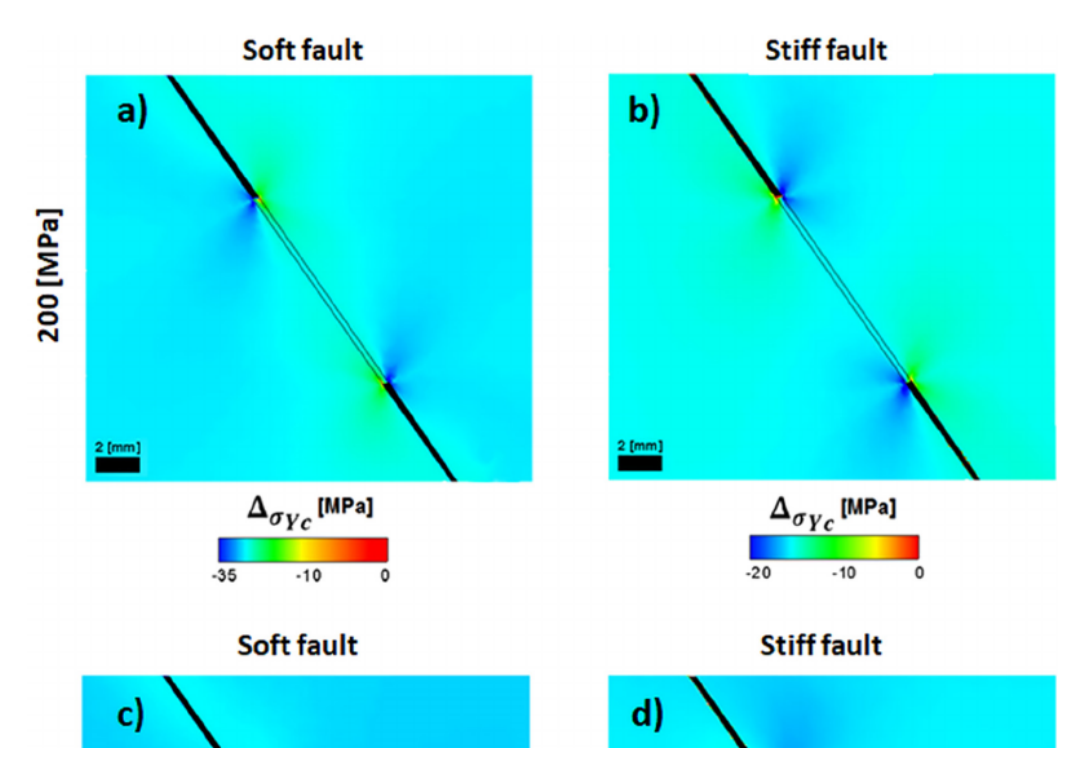
and 100 MPa experiments in association with planar faults (Figs. 10 and 11).

At an effective pressure of 200 MPa, the pre-existing fault in our experiment was effectively locked. Thus, the aforementioned mechanisms for 50–150 MPa experiments is less effective, since it requires fault movement in order to create a difference in stress concentration along specific areas. Nicol et al. (2013) suggested that stresses concentrated at geometrical irregularities, such as fragmented faulting, changes in lithology and intersections of conjugate faults, may be the cause of

deformation bands' tendency to cluster in zones of deformation bands, with no need for a shear strengthening mechanism. This fits our experimental observations of compaction band formation associated with fault geometry anomalies at high effective pressures.

Thus, we suggest that both shear strengthening and geometrical irregularities may have an important role in producing compaction bands associated with faults at different stages. When the movement on the pre-existing faults in sandstone is limited, the geometrical irregularities along the faults play a significant role in producing stress

12



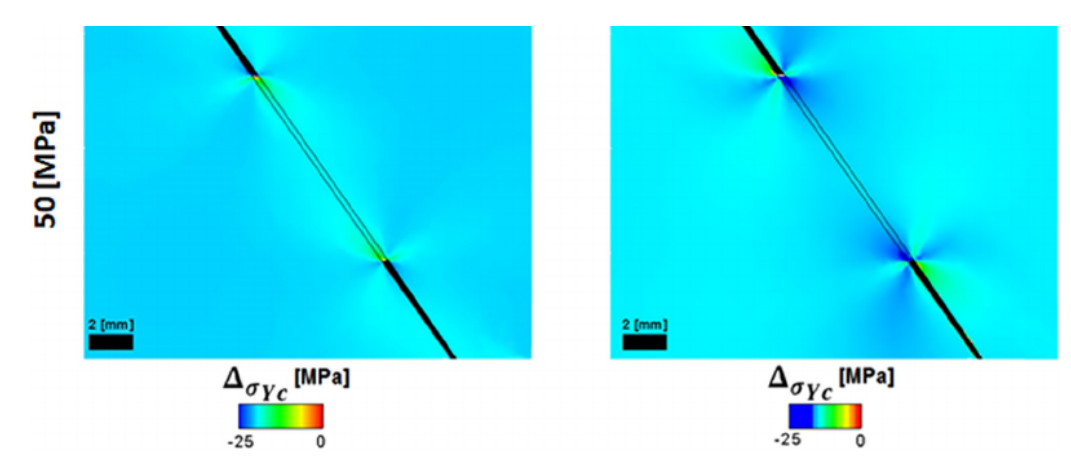


Fig. 14. Cross sections of cylinders showing $\Delta \sigma_{Yc}$ (the stress difference in a *Q-P* diagram between the stress state and the yield cap) calculated by a 3D COMSOL simulation of an axially deformed pre-faulted sandstone. The fault is segmented. (a) A stiff fault at a confining pressure of 200 MPa. (b) A soft fault at a confining pressure of 50 MPa. (c) A stiff fault at a confining pressure of 50 MPa.

concentrations, allowing the formation of compaction localization. However, when the fault is active, the non-homogeneous properties of the fault, mainly the difference in average grain size along it, creates a difference in the shear resistance that induces stress concentration at various points along it, inducing the formation of compaction bands. We further suggest that when a certain outcrop or drill core features abundant compaction bands associated with faults this may indicate to the presence of a large amount of stress concentrations along a given fault system.

In conclusion, we present evidence that compaction bands in Makhtesh Katan, Israel, formed as a result of the activity of pre-existing faults. We also presented experimental evidence of pre-existing faults inducing the formation of compaction bands by causing local stress concentrations. These results suggest that the presence of pre-existing faults, as well as other irregularities that may induce local stress concentrations, can explain the formation of compaction bands in the field under relatively low pressures.

On the basis of these results, we suggest that when movement on the fault is restricted (a condition that in our experiments occurred at high confining pressures of over 150 MPa), the fault geometry plays a substantial role in inducing local stress concentrations; when the fault is active, heterogeneous friction resistance along the fault, caused by local

13

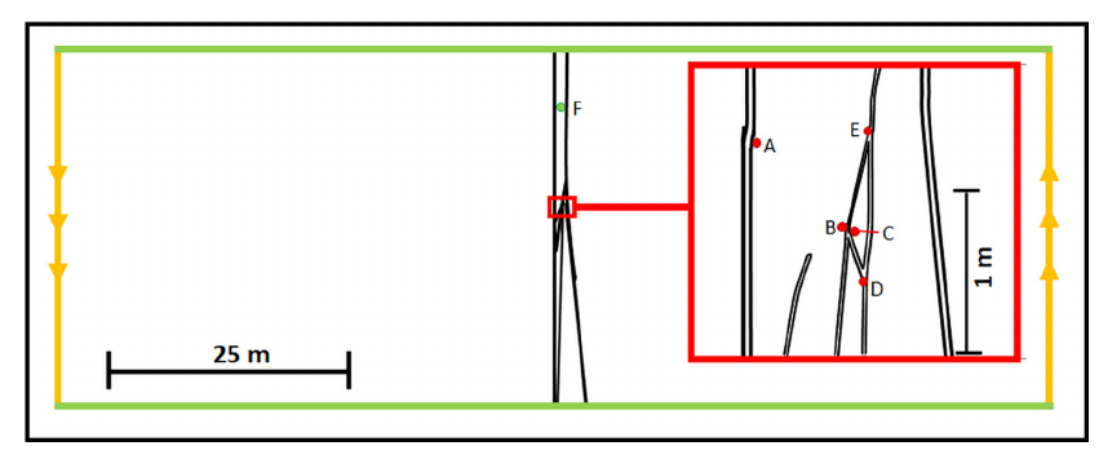


Fig. 15. COMSOL model boundary conditions of a simulation representing Site 1. The side boundaries, marked in orange, are displacement boundaries displaced by an equal amount on opposing directions marked by arrows (0.021, 0.02425, 0.0275, 0.0305 and 0.0335 [m] on each orange boundary). The top and bottom boundaries, marked in green, are free. The fault boundaries are marked in black and did not have any direct boundary conditions imposed on them. The fault areas were given a lower shear modulus compared to their surroundings. The mapped area of the outcrop is marked by a red square and enlarged. Red points A–E mark observation points in the areas with the highest stress concentrations. Green point F marks an observation point far from the compaction band formation area. (For interpretation of the references to color in this figure legend, the reader is referred to the web version of this article.)

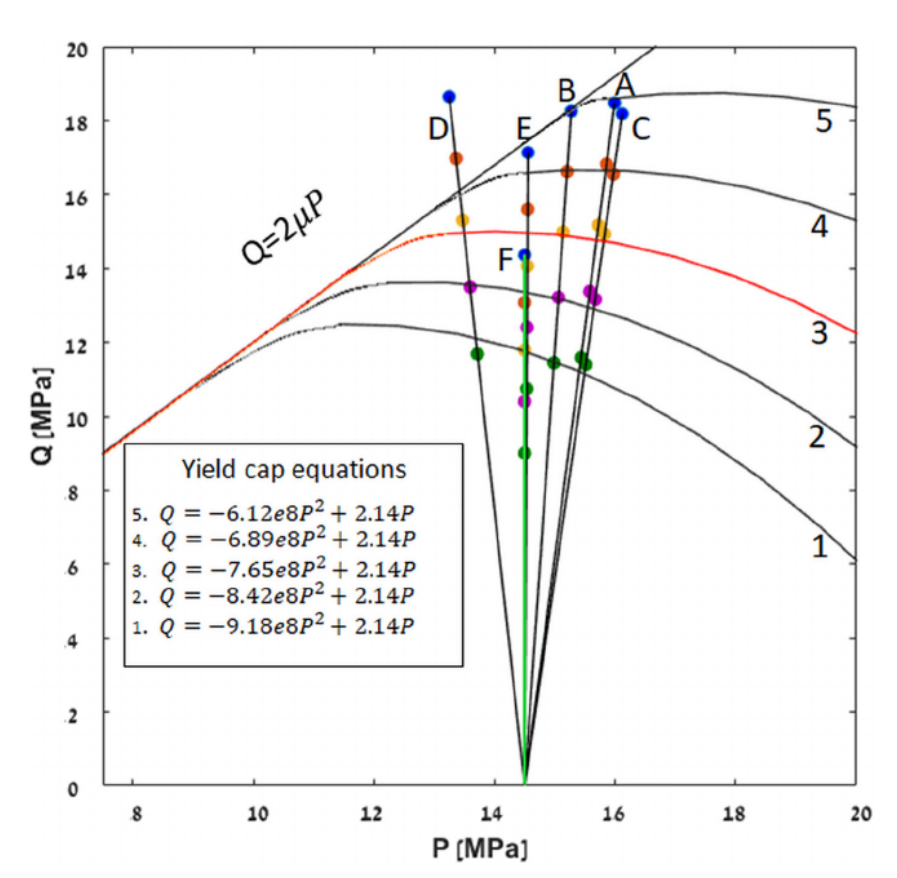
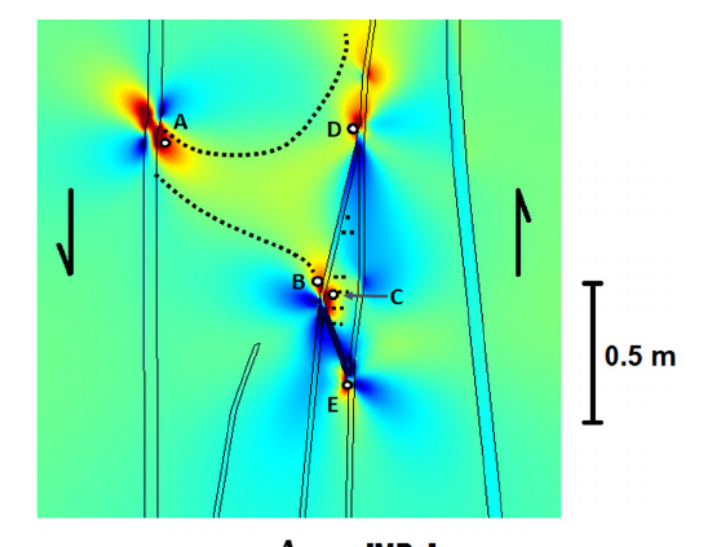


Fig. 16. Q-P diagram showing the deformation path of 6 points in the simulated Site 1 outcrop, along with several possible yield caps (the chosen yield cap marked in red). Markers of different colors along the deformation paths represent simulations with varying displacement along the boundary conditions (green = $5.8e^{-4}$, purple = $6.7e^{-4}$, yellow = $7.6e^{-4}$, red = $8.4e^{-4}$ and blue $=9.1e^{-4}$ strain on the orange boundaries marked on Fig. 14). The fan of black lines (lines A-E) marks the deformation path of 5 observation points shown in Fig. 15, placed in the areas with the highest stress concentrations. The green line marks the deformation path of observation point F (Fig. 15) placed at a distance from the faults, representing the average stress conditions of the outcrop. (For interpretation of the references to color in this figure legend, the reader is referred to the web version of this article.)

14

H. Gaist et al. Tectonophysics 747–748 (2018) 1–15



COMSOL AB, 2006. COMSOL Multiphysics User's Guide, Stockholm.

Deng, S., Aydin, A., 2012. Distribution of compaction bands in 3D in an aeolian sandstone: the role of cross-bed orientation. Tectonophysics 574, 204–218. https://doi. org/10.1016/j.tecto.2012.08.037.

Dresen, G., Stanchits, S., Rybacki, E., 2010. Borehole breakout evolution through acoustic emission location analysis. Int. J. Rock Mech. Min. Sci. 47, 426–435.

Eichhubl, P., Hooker, J.N., Laubach, S.E., 2010. Pure and shear-enhanced compaction bands in Aztec Sandstone. J. Struct. Geol. 32, 1873–1886. https://doi.org/10.1016/j. isg.2010.02.004.

Eran, G., 1982. Geology of Monoclines in the Negev. The Hebrew University, Jerusalem-Msc.

Fortin, J., Stanchits, S., Dresen, G., Guéguen, Y., 2006. Acoustic emission and velocities associated with the formation of compaction bands in sandstone. J. Geophys. Res. Solid Earth 111 (B10).

Fossen, H., 2010. Structrual Geology. Cambridge University Press, Cambridge.

Fossen, H., Schultz, R.A., Shipton, Z.K., Mair, K., 2007. Deformation Bands in Sandstone: A Review. vol. 164. pp. 755–769. https://doi.org/10.1144/0016-76492006-036.

Fossen, H., Schultz, R.A., Torabi, A., 2011. Conditions and implications for compaction band formation in the Navajo Sandstone, Utah. J. Struct. Geol. 33, 1477–1490. https://doi.org/10.1016/ji.jsg.2011.08.001.

Fossen, H., Zuluaga, L.F., Ballas, G., Soliva, R., Rotevatn, A., 2015. Contractional deformation of porous sandstone: Insights from the Aztec Sandstone, SE Nevada, USA. J. Struct. Geol. 74, 172–184.

Haimson, B., 2007. Micromechanisms of borehole instability leading to breakouts in rocks. Int. J. Rock Mech. Min. Sci. 44, 157–173.

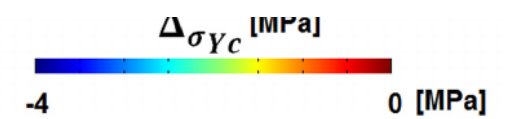


Fig. 17. Distribution of $\Delta \sigma_{Yc}$ (the stress difference in a *Q-P* diagram between the stress state and the yield cap). The black dotted line marks a zone in which wavy deformation bands might form. White circles represent observation points A–E, marked in red in Fig. 15.

variation in grain size and porosity, is also a major cause for fault related stress induced compaction localization.

Acknowledgements

We appreciate the helpful comments of the editor Dr. Rob Govers and the reviewers Mr. Martijn van den Ende and an anonymous reviewer. We thank Raphael Yacob and Swaed Iyad for their help with the field work. This work was funded by the U.S. Israel Binational Science Foundation (2014036). Partial support for WZ from NSF EAR-1761912 is acknowledged.

References

- Arkin, Y., Hamaoui, M., 1967. The Judea Group (Upper Cretaceous) in the central and southern Israel. In: Geological Society of Israel Bulletin. vol. 42. pp. 17.
- Aydin, A., 1978. Small faults formed as deformation bands in sandstone. Pure Appl. Geophys. 116, 913–930.
- Aydin, A., Ahmadov, R., 2009. Bed-parallel compaction bands in aeolian sandstone: their identification, characterization and implications. Tectonophysics 479, 277–284. https://doi.org/10.1016/j.tecto.2009.08.033.
- Aydin, A., Johnson, A.M., 1978. Development of faults as zones of deformation bands and as slip surfaces in sandstone. Pure Appl. Geophys. 116, 931–942.
- Aydin, A., Johnson, A.M., 1983. Analysis of faulting in porous sandstones. J. Struct. Geol. 5, 19–31.
- Aydin, A., Borja, R.I., Eichhubl, P., 2006. Geological and mathematical framework for failure modes in granular rock. J. Struct. Geol. 28, 83–98. https://doi.org/10.1016/j. isg.2005.07.008.
- Ballas, G., Soliva, R., Sizun, J.P., Fossen, H., Benedicto, A., Skurtveit, E., 2013. Shear-enhanced compaction bands formed at shallow burial conditions; implications for fluid flow (Provence, France). J. Struct. Geol. 47, 3–15. https://doi.org/10.1016/j.jsg.2012.11.008.
- Baud, P., Klein, E., Wong, T., 2004. Compaction localization in porous sandstones: spatial evolution of damage and acoustic emission activity. J. Struct. Geol. 26, 603–624. https://doi.org/10.1016/j.jsg.2003.09.002.
- Baud, P., Vajdova, V., Wong, T.F., 2006. Shear-enhanced compaction and strain localization: inelastic deformation and constitutive modeling of four porous sandstones. J. Geophys. Res. Solid Earth 111 (B12). https://doi.org/10.1029/2005JB004101.
- Charalampidou, E.M., Stanchits, S., Dresen, G., 2017. Compaction bands in a porous sandstone sample with pre-induced shear bands. In: International Workshop on Bifurcation and Degradation in Geomaterials. Springer, Cham, pp. 391–398.

- Hirsch, 1995. Geological map of Israel 1:50,000, sheet 19-ii, HaMakhtesh HaQatan. In: Geological Survey of Israel.
- Issen, K., Rudnicki, 2000. Conditions for compaction bands in porous rock. J. Geophys. Res. Solid Earth 105 (B9), 21529–21536.
- Katz, Y., Weinberger, R., Aydin, A., 2004. Geometry and kinematic evouloution of Riedel shear structures, Capitol Reef National Park, Utha. J. Struct. Geol. 26, 491–501.
- Klein, E., Baud, P., Reuschlé, T., Wong, T.F., 2001. Mechanical behavior and failure mode of Bentheim under triaxial compression. Phys. Chem. Earth 26, 21–25.
- Krenkel, E., 1924. Der Syrische Bogen Zentralbl. Fortschr. Mineral. 9, 274-281.
- Lyakhovsky, V., Zhu, W., Shalev, E., 2015. Visco-poro-elastic damage model for brittle-ductile failure of porous rocks. J. Geophys. Res. 120 (4), 2179–2199. https://doi.org/10.1002/2014JB011805.
- Mollema, P.N., Antonellini, M.A., 1996. Compaction bands: a structural analog for anti-mode I cracks in aeolian sandstone. Tectonophysics 267, 209–228. https://doi.org/10.1016/S0040-1951(96)00098-4.
- Nicol, A., Childs, C., Walsh, J.J., Schafer, K.W., 2013. A geometric model for the formation of deformation band clusters. J. Struct. Geol. 55, 21–33.
- Reches, Z.E., 1976. Analysis of joints in two monoclines in Israel. Geol. Soc. Am. Bull. 87, 1654–1662.
- Schultz, R.A., Siddharthan, R., 2005. A general framework for the occurrence and faulting of deformation bands in porous granular rocks. Tectonophysics 411 (1–4), 1–18.
- Shamir, G., Eyal, Y., 1995. Elastic modeling of fault-driven monoclinal fold patterns. Tectonophysics 245 (1–2), 13–24.
- Sneh, A., Weinberger, R., 2014. Major Structures of Israel and Environs, Scale 323 1:50,000. Israel Geological Survey, Jerusalem.
- Soliva, R., Ballas, G., Fossen, H., Philit, S., 2016. Tectonic regime controls clustering of deformation bands in porous sandstone. Geology 44 (6), 423–426.
- Tembe, S., Vajdova, V., Wong, T.F., Zhu, W., 2006. Initiation and propagation of strain localization in circumferentially notched samples of two porous sandstones. J. Geophys. Res. Solid Earth 111 (B2), B02409. https://doi.org/10.1029/ 2005JB003611.
- Vajdova, V., Baud, P., Wong, T.F., 2004. Permeability evolution during localized deformation in Bentheim sandstone. J. Geophys. Res. Solid Earth 109 (B10).
- Weinberger, R., Baer, G., Shamir, G., Agnon, A., 1995. Deformation bands associated with dyke propagation in porous sandstone, Makhtesh Ramon, Israel. In: Baer, G., Heimann, A. (Eds.), The Physics and Chemistry of Dykes. 33. Balkema, Rotterdam, pp. 95–112.
- Weinberger, R., Lyakhovsky, V., Baer, G., Agnon, A., 2000. Damage zones around en echelon dike segments in porous sandstone. J. Geophys. Res. Solid Earth 105 (B2), 3115–3133.
- Weissbrod, T., 1993. Lithology and stratigraphy of Lower Cretaceous formations in the southern Negev (Elat region). In: Israel Geological Survey, Current Research. vol. 8. pp. 62–64.
- Wong, T.F., Baud, P., Klein, E., 2001. Localized failure modes in a compactant porous rock. Geophys. Res. Lett. 28 (13), 2521–2524.
- Yechieli, Y., Elron, E., Sneh, A., 1994. Geological Map of Israel, 1: 50,000 (Sheet 19–IV, 20–III) Neot Hakikar. Geol. Surv. Isr.
- Zhu, W., 2007. Faulting Related Initiation and Growth of Compaction Localization in Porous Sedimentary Rocks, AGU-Geophysical Research Abstracts (9).
- Zhu, W., Montési, L., Wong, T.F., 2002. Influence of loading path on anisotropic damage and permeability evolution during mechanical compaction of sandstone. In: de Meer, S., Drury, M.R., de Bresser, J.H.P., Pennock, G.M. (Eds.), Deformation Mechanisms, Rheology and Tectonics: Current Status and Future Perspectives. Geological Society, London, Special Publications, vol. 200. pp. 119–136.
- Zhu, W., Montési, L., Wong, T.F., 2007. A probabilistic damage model of stress-induced permeability anisotropy during cataclastic flow. J. Geophys. Res. 112, B10207. https://doi.org/10.1029/2006JB004456.